



# Design of robust particle dampers using inner structures and coated container walls

Niklas Meyer<sup>1</sup> · Robert Seifried<sup>1</sup>

Received: 15 November 2021 / Accepted: 6 December 2023  
© The Author(s) 2023

## Abstract

Classical particle dampers suffer from their non-robust damping behavior, i.e. they can only be efficiently applied to a specific frequency range and amplitude range. The reason for that is that particle motion, also called motion mode, and damper efficiency show a strong correlation. By changing particle or container properties the motion modes are shifted to other excitation conditions but their efficient range is not much affected. To increase the damping performance and robustness of particle dampers, two approaches are presented here by introducing new motion modes. Therefore, the particle dampers are analyzed experimentally using a shaker setup and numerically using the discrete element method. The first design approach uses inner structures inside the particle damper, manufactured by a 3D printer. The inner structures consist of different numbers of beams, placed perpendicular to the container moving direction. They lead to a much more robust damper as the transition between the motion modes gets smoother. For the second approach, the container walls are equipped with different soft polymers. In this way a new motion mode at low excitation intensities is observed, leading to a high efficiency possibly on a large excitation intensity range. For an easy calculation of the necessary wall's Young's modulus an analytical formula based on Hertz impact theory is derived.

**Keywords** Particle damper · Inner structures · Coated container walls · DEM · Design guidelines

## 1 Introduction

Passive damping techniques are often applied to reduce structural vibrations. Classical liquid dampers are most widely used for these applications. These dampers are well studied and mathematically easy to describe. However, liquid dampers fail under harsh environmental conditions and do need an anchor point. Hence, especially for applications where liquid dampers are not suitable, *particle dampers* are becoming more and more popular.

Here, containers filled with granular material are attached to the vibrating structure. Via structural vibrations, momentum is transferred to the particles causing granular

interactions. Inelastic normal collisions and frictional losses lead to energy dissipation, reducing the structural vibration [24]. On the one hand, particle dampers show various advantages compared to other damping techniques. Especially, the ability to withstand harsh environmental conditions [25, 32] and the high durability [11] are major benefits. Additionally, they are cost-efficient devices and add only little mass to the primary system, as shown by Johnson [11]. Also, particle dampers lead to broadband damping properties, see e. g. Schönle [31]. On the other hand, so far no general design guidelines exist, hindering their wide industrial usage. This is because particle motion, also referred to as *motion mode*, and *energy dissipation* correlate in a non-trivial way, which is often poorly understood. Identifying these correlations is still part of ongoing research, see e. g. [15, 21, 28, 36, 37].

To obtain a better understanding of the complex mechanisms inside particle dampers, the *discrete element method* (DEM) is widely applied. The DEM has been developed by Cundall and Strack [4] for the simulation of granular systems consisting of discs and spheres. Nowadays, arbitrary particle shapes can be simulated,

---

✉ Niklas Meyer  
n.meyer@tuhh.de

Robert Seifried  
robert.seifried@tuhh.de  
https://www.tuhh.de/mum

<sup>1</sup> Institute of Mechanics and Ocean Engineering, Hamburg  
University of Technology, Eißendorfer Straße 42,  
21073 Hamburg, Germany

see Lu et al. [13] or Matuttis [16]. However, for reasons of numerical efficiency spherical particles are still most commonly used. The particle dynamics are mainly influenced by particle interactions. Therefore, various contact models have been developed. The applied penalty laws can but do not need to be based on physical laws, see e. g. Pöschel [26].

For monodisperse spherical particle systems, an intensive study about the correlation of particle motion modes and energy dissipation is presented by the authors in [21] for a wide excitation frequency range and excitation amplitude range. The motion mode of a particle bed describes its current state of movement, e. g. the fluidization mode for fluid-like motion or the bouncing collect-and-collide state for a movement as one particle block. It is shown how particle properties, container properties and micro-mechanical contact behavior influence the efficiency of the different motion modes. However, the efficient range within the motion modes concerning excitation frequency and excitation amplitude is limited by the studied influence parameters.

To overcome this problem, in literature various approaches have been studied. Hollkamp [10] experimentally found only little effect of the particle shape. Numerical studies by Hamzeh [27] came to the same conclusion. Moreover, geometrically simple container shapes, like cuboids or cylinders, as well as their orientation seem to be of minor importance, as found by the authors [21]. More complex container shapes, however, could have a significant influence, see Wong et al. [33]. An interesting approach is presented by Gnanasambandham [7] who uses liquid-filled particle dampers to damp low frequency vibrations and achieved good results. Another design is presented by Yao [35]. He equipped the particle dampers with lose spoilers to increase the damping performance at small vibration amplitudes. This approach is adopted by Gnanasambandham [6] to fixed inner structures. Thereby, an increased damping performance at a single frequency is obtained. By Lu et al. [14] as well as Li and Darby [12] coated particle dampers for application in civil engineering are investigated. These dampers show significantly lower force peaks caused by the particles and could increase the damping performance.

Although many promising approaches to increase the damping performance and excitation robustness of particle dampers exist, accurate design guidelines are still missing. This is because the investigations are often restricted to numerical analysis or a single excitation frequency. Hence, the overall picture is not obtained and general statements are difficult to derive. This paper aims to partly close this gap by presenting extensive numerical and experimental studies for horizontal vibrations of high excitation intensities. Hereby general design guidelines for the design of robust particle dampers are derived. Especially, *coated container walls* and *fixed inner structures* are used to fulfill this task.

This paper is organized in the following way: First, in Sect. 2 the different characterization methods for particle dampers, i. e. motion modes and the complex power method, are introduced briefly. In the following Sect. 3 the experimental and numerical setups are introduced. The obtained insights and design guidelines are then presented in Sect. 4. Finally, the conclusion is given in Sect. 5.

## 2 Characterization methods

To analyze *motion modes* and the *energy dissipation* of a particle damper, the damper is investigated separately, i. e. without underlying structure. Thus, general insights can be obtained either from experiments or simulations. The particle damper is subjected to a defined horizontal vibration using a rheonomic constraint, i. e. it follows the given movement perfectly. The particle container movement is applied as

$$x_c = X \sin(\Omega t), \quad (1)$$

with container amplitude  $X$  and angular frequency  $\Omega = 2\pi f$ . The corresponding container velocity and acceleration follow as

$$\dot{x}_c = V \cos(\Omega t), \quad (2)$$

$$\ddot{x}_c = -A \sin(\Omega t), \quad (3)$$

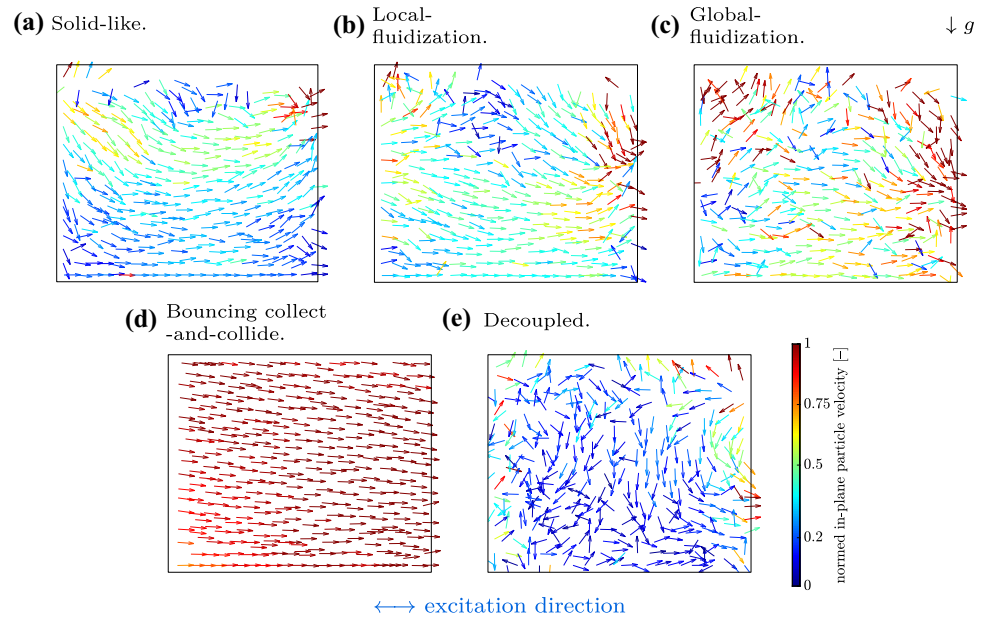
with  $V = X\Omega$  and  $A = X\Omega^2$ . Oftentimes, the dimensionless excitation intensity  $\Gamma = A/g$  is used, with  $g$  as gravity constant.

### 2.1 Motion modes

To distinguish the different motion modes of a particle damper, animations, velocity fields and experimental observations can be used. Indeed, this task is not always trivial and unambiguous as the transition between motion modes is smooth. By the authors five different motion modes are observed for a monodisperse particle system under horizontal vibration, see [21]. The velocity fields of these motion modes are shown in Fig. 1 for the in-plane particle velocity in the direction of excitation and gravity. All velocity fields are taken at a container position of  $x_c = X$ , i. e. at the maximum stroke and zero container velocity.

The *solid-like state*, see Fig. 1a and Meyer and Seifried [21], is characterized by almost no relative motion between particles and container. This causes the granular matter to look like an added block, staying at the container base and moving with the same velocity as the container. Here, this motion mode is seen at low excitation intensities up to  $\Gamma \approx 1$ .

**Fig. 1** Velocity fields of motion modes at  $x_c = X$ . The colors show the magnitude of the in-plane particle velocity normed by the container velocity amplitude  $V$  from low (blue) to high (red)



For excitation intensities  $\Gamma \geq 1$  the granular systems first enters a state of *local-fluidization*, see Fig. 1b and Saluena [29]. Particles located at the top layers become fluidized, i. e. irregular relative motion between these particles, while the particles at the container bottom still behave like a solid. When the excitation intensity is further increased the whole particle system gets fluidized, called *global-fluidization*, as shown in Fig. 1c and by Saluena [29].

From the global-fluidization, depending on the excitation conditions the particle system can migrate in different motion modes, like bouncing collect-and-collide, decoupled, convection or Leidenfrost effect. For the here investigated particle dampers, only the *bouncing collect-and-collide* and *decoupled motion modes* are observed. In the bouncing collect-and-collide motion mode, see Fig. 1d and Sack et al. [28], the particles move as one single particle block synchronously with the driven container and collide inelastically with the damper walls. The decoupled motion mode is shown in Fig. 1e and by Meyer and Seifried [21]. This motion mode also migrates from the global-fluidization. It is characterized by a very small absolute particle velocity compared to the velocity of the container. Thus, the granular matter appears to be decoupled from the container.

## 2.2 Complex power

To analyze the *energy dissipation* and the *efficiency* of the particle damper, the *complex power method*, introduced by Yang [34], is used. The complex power is determined by

$$P^* = \frac{1}{2} F^* \bar{V}^{*\top}. \quad (4)$$

At this,  $F^*$  denotes the complex amplitude by *fast Fourier transform* (FFT) of the driving force signal acting on the container and  $\bar{V}^*$  is the conjugate complex amplitude by FFT of the velocity signal of the container motion. Both quantities can be obtained from experiments or simulations. The dissipated energy per cycle  $\tilde{E}_{\text{diss}}$  then follows using the complex power to

$$\tilde{E}_{\text{diss}} = 2\pi E_{\text{diss}} = \frac{2\pi}{\Omega} \cdot \text{Real}(P^*). \quad (5)$$

To judge the damper's efficiency the *effective loss factor*  $\bar{\eta}$  is used, see Masmoudi et al. [15] and Meyer and Seifried [21] for details. It is calculated by a scaling of the dissipated energy with the kinetic energy of the particle system  $E_{\text{kin}}$  using the mass of the particle bed  $m_{\text{bed}}$ , i. e. the mass of all particles, to

$$\bar{\eta} = \frac{E_{\text{diss}}}{E_{\text{kin}}} = \frac{E_{\text{diss}}}{\frac{1}{2} m_{\text{bed}} |V_{\Omega}^*|^2}, \quad (6)$$

with  $V_{\Omega}^*$  being the complex amplitude by FFT of the velocity signal at driving frequency. As consequence, the effective loss factor is independent of the container and particle mass and enables the comparison of different particle settings. It should be noted that do to the definition of the effective loss factor, it is not limited by a value of one. However, to compare different particle damper settings and to ensure a unique coloring of the later utilized surface plots, a value of one or higher is indicated by the same color.

### 3 Experimental and numerical setup

#### 3.1 Experimental setup

For the analysis of the energy dissipation and effective loss factor, a corresponding testbed is set up by the authors in [18, 19] and shown in Fig. 2.

In this paper, the particle container is an aluminum cylinder with an inner radius  $R$  of 20 mm and an adjustable length  $L$  of  $50 \pm 5$  mm. To realize the adjustable length, the container and the cap of the container are equipped with a fine thread. This adjustable length of the cylinder will be used later to set up the clearance  $h$  between particle bed and container cap precisely, see also Fig. 2-left. Experimental tests performed here have shown that the minimum clearance is limited by the particle radius, i.e.  $h_{\min} \approx r$ . This limitation might be due to the irregular surface of the particle bed. Hence, the fine-tuning of the clearance is performed by experimental tests, as the clearance can also be extracted from the measurement results. This is explained later in detail. The mass of the container is  $m_{\text{con}} = 200$  g. To realize the rheonomic constraint of the container movement, see Eq. (1), the particle damper is excited by a controlled harmonic force via a shaker, the *LDS V455*, perpendicular to gravity. The shaker's excitation force is controlled in order for the frequency and acceleration magnitude of the container to stay constant. For this, the container's acceleration is measured by the *4534-B* accelerometer and processed by the *LDS Comet* system. The excitation force is measured using a load cell, the *8230-002*. Shaker, accelerometer, load cell and control system are from BRÜEL & KJÆR. The velocity of the particle container is measured via a laser vibrometer (LV) *PSV-500* from POLYTEC. The data acquisition of the velocity and force signals are accomplished by the Front-End of the *PSV-500* with a sampling frequency of 40 kHz.

The feasible measurement range of the experimental setup lies between excitation frequencies of 40 Hz to 1 kHz and between excitation amplitudes of  $1 \leq \Gamma \leq 40$ .

The measurement range is divided up into a logarithmic grid of 108 points. Hence, 12 frequencies and 9 acceleration values are used and each combination is measured for a duration of 5 s.

#### 3.2 Numerical model

To study the particle damper numerically the *discrete element method* (DEM), developed by Cundall and Strack [4], is used. It is a discrete simulation method for granular materials. Every particle is considered as an unconstrained moving body only influenced by applied forces. The dynamics are described by *Newton's and Euler's equation of motion* for every particle, see e. g. Pöschel [26], and are mainly influenced by contacts between particles themselves and walls. The absolute translational acceleration of the center of mass  $\ddot{\mathbf{x}}_i = [\ddot{x}_i^x, \ddot{x}_i^y, \ddot{x}_i^z]^T$  of particle  $i$  is obtained by

$$m_i \ddot{\mathbf{x}}_i = \mathbf{f}_{a,i}, \quad (7)$$

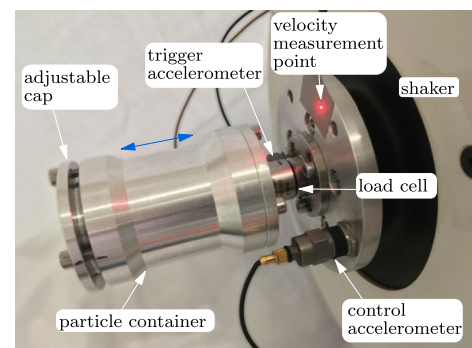
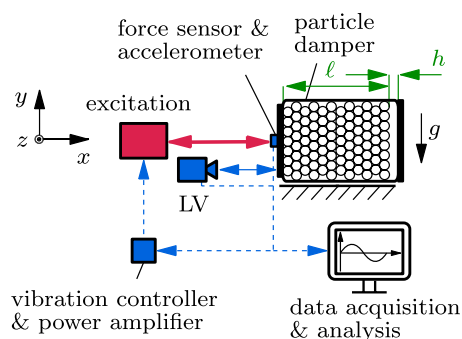
with particle mass  $m_i$  and  $\mathbf{f}_{a,i}$  being the vector of applied forces on particle  $i$ . Since only spherical particles are considered in this work, the rotational acceleration  $\dot{\boldsymbol{\omega}}_i = [\dot{\omega}_i^x, \dot{\omega}_i^y, \dot{\omega}_i^z]^T$  of particle  $i$  is calculated as

$$\mathbf{I}_i \dot{\boldsymbol{\omega}}_i = \boldsymbol{\ell}_{a,i}, \quad (8)$$

with the particle's inertia tensor  $\mathbf{I}_i$  and  $\boldsymbol{\ell}_{a,i}$  being the vector of applied torques on particle  $i$  in respect of the particle's center of mass. The inertia tensor  $\mathbf{I}_i = I_i \mathbf{E}$  of the particles is diagonal, whereby all three entries of  $\mathbf{I}_i$  are identical. To model a contact, the contact partners' mutual compression is used. This modeling allows the contact partners to deform continuously. The mutual compression  $\delta$  is counteracted by the resulting contact forces.

In this research, the algorithms presented by the authors in [20] are used for the spherical particles. At every new time step, the contact detection is performed. All existing contacts have to be determined. If every particle is checked with all others this results in a search complexity of  $\mathcal{O}(n_p^2)$ , with  $n_p$  being the total number of particles. A variety of algorithms have been developed to increase the search

**Fig. 2** Testbed for determination of energy dissipation of particle dampers with schematic representation (left) and picture (right)



efficiency, such as sort-based, cell-based, or tree-based ones, decreasing the search complexity to an optimum of  $\mathcal{O}(n_p)$ . In the program, the Verlet list in combination with the link cell algorithm are used, as described in detail by Pöschel [26].

For the normal contact forces the formula of Gonthier [8] is utilized and reads

$$F_n = k_n \delta^{3/2} \left( 1 + \frac{\bar{d}}{\varepsilon} \frac{\dot{\delta}}{\dot{\delta}_0} \right). \quad (9)$$

It is based on the contact law of Hertz [9] using physical parameters of the contact partners to describe the contact stiffness  $k_n$ , namely the particle radius  $r$ , the Young's modulus  $E$ , and the Poisson's ratio  $\nu$ . The damping during contact is modeled using the penetration velocity  $\dot{\delta}$  and the initial penetration velocity  $\dot{\delta}_0$ . The non-linear damping parameter  $\bar{d}$  depends only on the *coefficient of restitution* (COR)  $\varepsilon$  and can be solved offline, see Gonthier [8]. The COR controls the amount of energy dissipation during contact. For  $\varepsilon = 1$  the contact procedure is fully elastic, while for  $\varepsilon = 0$  the contact procedure is fully inelastic. Here, a velocity dependent COR is applied, which has been determined by previous numerical *finite element method* (FEM) studies, see [23]. The utilized COR is displayed in Fig. 3 for the later used steel sphere–sphere impacts as well as for steel sphere–aluminum

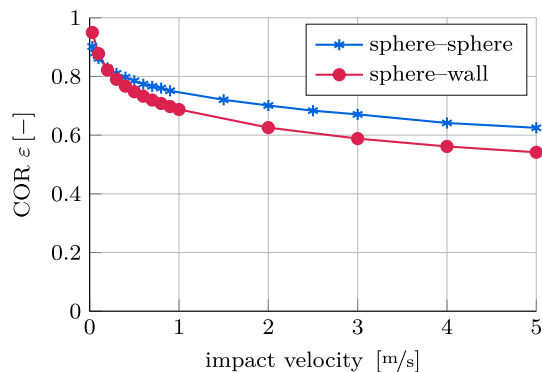


**Fig. 3** COR of steel sphere–sphere and steel sphere–aluminum wall impacts by FEM simulations for a particle radius of 1.25 mm

wall impacts and a particle radius of 1.25 mm. For both contact pairs, a high dependency on impact velocity is observed. For very small impact velocities, the COR is close to one. When the impact velocity increases the COR starts to decrease rapidly for both contact pairs. For high impact velocities, the COR drops below 0.63 and 0.54, respectively, and converges to an almost constant value.

For the tangential forces, sliding friction using a smoothing hyperbolic tangent function to avoid jumps in the friction forces at zero velocity is utilized, which is presented by Andersson et al. [1] and reading

$$F_t = -\mu |F_n| \cdot \tanh(\tau |v_p^t|), \quad (10)$$

with  $\mu$  being the friction coefficient,  $v_p^t$  being the relative, tangential velocity at the contact point of the collision partners and  $\tau$  the smoothing parameter.

The chosen time integrator has a big influence on the simulation speed and the overall stability. As the contact detection and evaluation of the contact forces are most time-consuming in DEM simulations, the numerical effort for the time integrator itself is often negligible. But, its choice has a big influence on the number of evaluations of the equation of motion. Here, the time integration is performed using a variable time step fifth order Gear predictor-corrector algorithm developed by Gear [5] and presented in detail in Meyer and Seifried [20].

The accuracy of the implemented simulation code in MATLAB has been validated several times, see e. g. [21, 22]. For the desired simulation time of up to 1 s, the code runs very efficient for particles numbers up to 10,000 – 20,000. The used material and contact data are listed in Table 1. As in the experiments, the same excitation and post-processing parameters are chosen. Each excitation configuration is simulated for 25 vibration cycles.

## 4 Design of robust particle dampers

Within this paper, various particle damper designs are analyzed experimentally and compared with each other. Aside from that, numerical analyses are performed to gain further

**Table 1** Material parameters of spheres and container

Material	Sphere	Container
	S235	Al6060
Young's Modulus [GPa]	208	70
Poisson's Ratio [–]	0.3	0.33
Density [kg/m <sup>3</sup> ]	7900	2700
Friction Coefficient [–]	0.1 for all contacts	
Coefficient of Restitution [–]	velocity dependent, see Fig. 3	
Dimensions [mm]	$r_p = 1.25$	$L, R = 50 \pm 5, 20$



insights into the complex processes inside particle dampers. To make the results comparable, a standardized approach is used. At that, the cylindrical particle damper is filled with spherical steel particles of 1.25 mm radius. For the filling procedure, the longitudinal axis of the damper points against gravity. Particles are poured up to a marking at  $\ell = 50$  mm, see Fig. 2-left. Thus, the damper contains about 4500 particles weighting about 291 g. Hence, a sufficient amount of particles exist in all container dimensions and a numerical analysis using DEM is still affordable. The adjustable cap of the cylindrical container is used to set up a clearance of  $h = \pi$  mm. The size of the clearance will be discussed in the next section. For the experiments the container is turned by  $90^\circ$ , so that the longitudinal axis of the cylinder is perpendicular to gravity and in the direction of excitation, see Fig. 2. This setting is henceforth referred to as *baseline setting*. Later, the effect of inner structures or coated container walls are analyzed, which consequently reduces the total amount of particles inside the damper. As the effective loss factor is independent of the container mass and particle mass, see Eq. (6), the results are still comparable.

#### 4.1 Baseline setting

The baseline setting is analyzed experimentally as well as numerically using DEM. The numerical accuracy of the DEM model is demonstrated by the authors in [21]. In Fig. 4 the effective loss factor of the baseline setting determined experimentally and the corresponding motion modes are shown. The motion modes are determined from animations and velocity fields obtained from simulation as well as indirectly from the experimentally measured effective loss factor. The latter is possible due to the strong correlation of effective loss factor and motion modes, see [21].

Different motion modes can be observed, depending on both the excitation frequency and excitation intensity. The solid-like state is only seen at the lowest acceleration intensity  $\Gamma = 1$  and low excitation frequencies  $f \leq 100$  Hz. The solid-like state, see also Fig. 1a, is classified by almost no relative motion between particles and container. This results in a low energy dissipation and causes the effective loss factor to be low  $\bar{\eta} < 0.1$ .

From the solid-like state, the system turns into the local-fluidization mode, see also Fig. 1b. The local-fluidization mode is seen for low acceleration intensities  $\Gamma \leq 2$  and low to medium excitation frequencies  $f = 40\text{--}250$  Hz. As most of the particles still behave like a solid and only the top particle layers show some relative motion, the effective loss factor is still comparatively low  $\bar{\eta} = 0.2\text{--}0.3$ .

From the local-fluidization mode, the system switches to the global-fluidization mode, see Fig. 1c. The global-fluidization mode can be observed on a large excitation range with low to high effective loss factor values  $\bar{\eta} = 0.2\text{--}1.6$ .

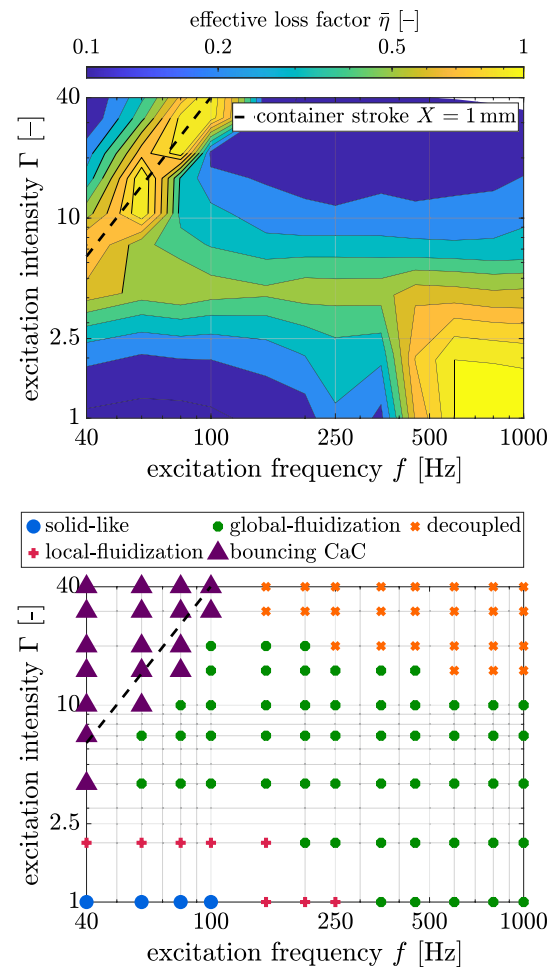


**Fig. 4** Experimentally obtained effective loss factor (*top*) and identified motion modes (*bottom*) of about 4500 steel particles of 1.25 mm radius. The dashed line indicates a constant container stroke of  $X = 1$  mm. CaC: collect-and-collide

Medium effective loss factor values occur at the transition from local to global-fluidization mode, at acceleration intensities of  $\Gamma \approx 3$ . This behavior can be explained by the transition to global-fluidization. Even though there is a substantial amount of relative motion between the particles, the total kinetic energy is still comparatively low. This results in the medium effective loss factor values. Further accelerating the container leads to an increase in relative motion and an even higher increase of kinetic energy, resulting in a reduction of the effective loss factor. However, at high excitation frequencies  $f > 500$  Hz and low excitation intensities  $\Gamma < 3$  effective loss factor values up to  $\bar{\eta} = 1.6$  are seen. In this regime, the kinetic energy of the particle bed is very low, because the container velocity amplitude  $V$  is low, see Eq. (2). However, the reason for the high measured effective loss factor values is not conclusively clarified, but might occur due to air resistance or cohesive forces. This is still under investigation.

The bouncing collect-and-collide and decoupled motion modes, see Fig. 1d and e, develop from the global-fluidization mode at high acceleration intensities  $\Gamma \geq 10$ . The decoupled motion mode occurs at medium to high excitation frequencies  $f \geq 150$  Hz and is characterized by a small effective loss factor  $\bar{\eta} = 0.05$ – $0.15$ . This is reasonable as the motion of the particle bed is decoupled from the container. Hence, only little energy is transferred to the particle bed, resulting in low energy dissipation.

The bouncing collect-and-collide mode on the other hand appears at low excitation frequencies  $f < 150$  Hz. The effective loss factor range is very large with  $\bar{\eta} = 0.1$ – $1.0$ . In the bouncing collect-and-collide motion mode, the particle bed forms a packed layer that takes off the container base, see Fig. 1e. This packed particle layer moves synchronously with the driven container as illustrated in Fig. 5.

At first, the particle bed is pushed by the container wall, until the container reaches its maximum velocity  $\dot{x}_c = V$ . At this point, the particle bed leaves the container wall and moves with constant velocity  $\dot{x}_{\text{bed}} = V$ . At impact with the opposite container wall, an inelastic collision occurs, i. e. the particle bed adopts the container's velocity instantaneously, see Sanchez et al. [30] and Bannerman et al. [2] for details. It is seen in Fig. 4 that the contour lines of the effective loss factor for this motion mode agree very well with the lines of constant container stroke, as indicated for  $X = 1$  mm. Thus, the effective loss factor of this motion mode is very sensitive to the container stroke. Bannerman [2] and Sack [28] derived a formula to calculate the container stroke at maximum effective loss factor. They obtain that the maximum effective loss factor is achieved when the particle bed impacts the opposite container wall when the container is moving in the other direction again with maximum velocity, i. e. at  $x_c = 0$  and  $\dot{x}_c = -V$ , see Fig. 5. The optimal container stroke of the bouncing collect-and-collide motion mode  $X_{\text{opt}}$  is therefore achieved to

$$X_{\text{opt}} = \frac{h}{\pi}, \quad (11)$$

with  $h$  being the clearance of the particle bed to the opposite container wall as indicated in Fig. 5. This is remarkable as

no dependency on the excitation frequency exists for the optimal stroke. For container strokes higher than the optimal one (above the dashed line in Fig. 4), the effective loss factor slowly decreases. However, for container strokes lower than the optimal one (below the dashed line in Fig. 4), the effective loss factor quickly decreases. This happens due to the transition into a different motion mode. See also the authors' other works [17, 21] for further discussion of this topic. Hence, the obtained result is sensitive to the container stroke and more robust designs are necessary.

By using the measured optimal stroke and Eq. (11) the clearance can be extracted from measurements and tuned in a targeted manner. Here, for the desired clearance of  $h = \pi$  mm an optimal stroke of  $X_{\text{opt}} = 1$  mm is obtained. Hence, for this optimal stroke, the bouncing collect-and-collide motion mode is clearly visible, see Fig. 4.

## 4.2 Inner structures

To increase the efficient range of operation of particle dampers, i. e. a more robust behavior concerning the stroke of the particle damper, different *inner structures* for the container are analyzed experimentally in the following. These inner structures are printed by the SLA 3D printer *Form3* by FORMLABS using the *Tough 2000* resin and a printing resolution of  $100 \mu\text{m}$ . In order for the structures to withstand the high impact forces applied by the particles, this especially strong and durable resin is chosen. Figure 6 shows the three different inner structures developed here.

The structures are printed with an included base plate for the cylindrical container and are attached to it by four screws. All arms of the structures have a cross section of  $5 \text{ mm} \times 5 \text{ mm}$ . The first structure, see Fig. 6a, is a *single cross* positioned in the middle of the cylinder. The second structure, shown in Fig. 6b, is a *triple cross* with three evenly distributed crosses connected to each other. Likewise, the last structure depicted in Fig. 6c is a *triple star* with uniform intervals between the stars. For the triple star setting the particle mass reduces from 291 to 220 g, which results still in a particle number of about 3400 instead of 4500. This is still sufficiently enough for all motion modes to appear.

**Fig. 5** Particle movement of the bouncing collect-and-collide motion mode at high effective loss factor values

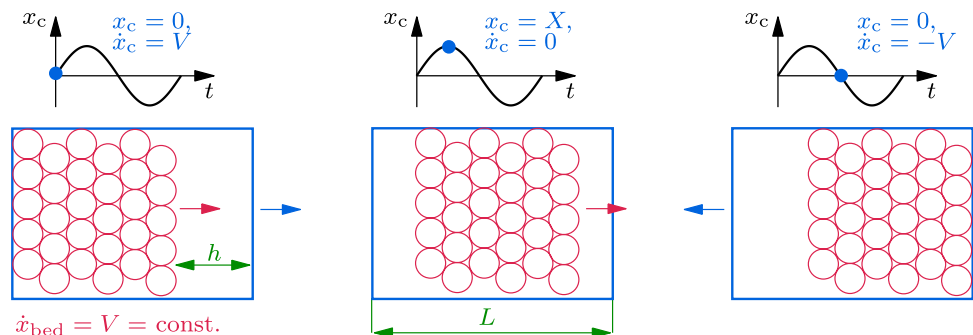
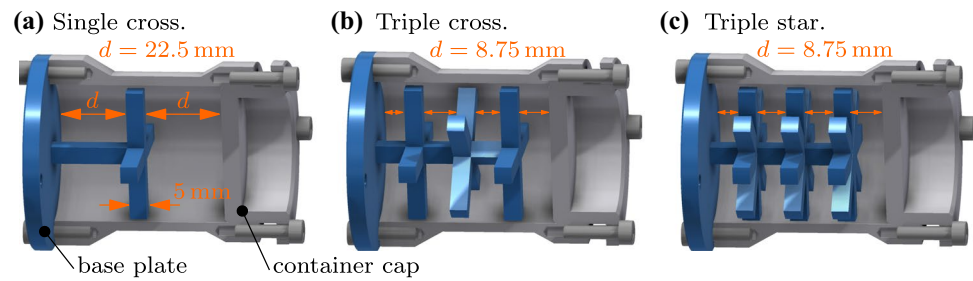


**Fig. 6** CAD sketches of inner structures inside cylindrical particle container



#### 4.2.1 Experimental results

The experimental results of the effective loss factor for these three structures filled with 1.25 mm radius steel spheres and a clearance of  $h = \pi$  mm are shown in Fig. 7. To enhance comparability, the result of the baseline setting of Fig. 4 is displayed as well.

A strong influence of the inner structures on the damping properties is visible. The use of more structural elements results in a greater impact on the damping characteristics. At the optimal stroke of the bouncing collect-and-collide motion mode, the effective loss factor decreases with increasing number of used inner structures. Starting at  $\bar{\eta} = 1.0$  for the baseline setting and reducing to  $\bar{\eta} = 0.8$  for

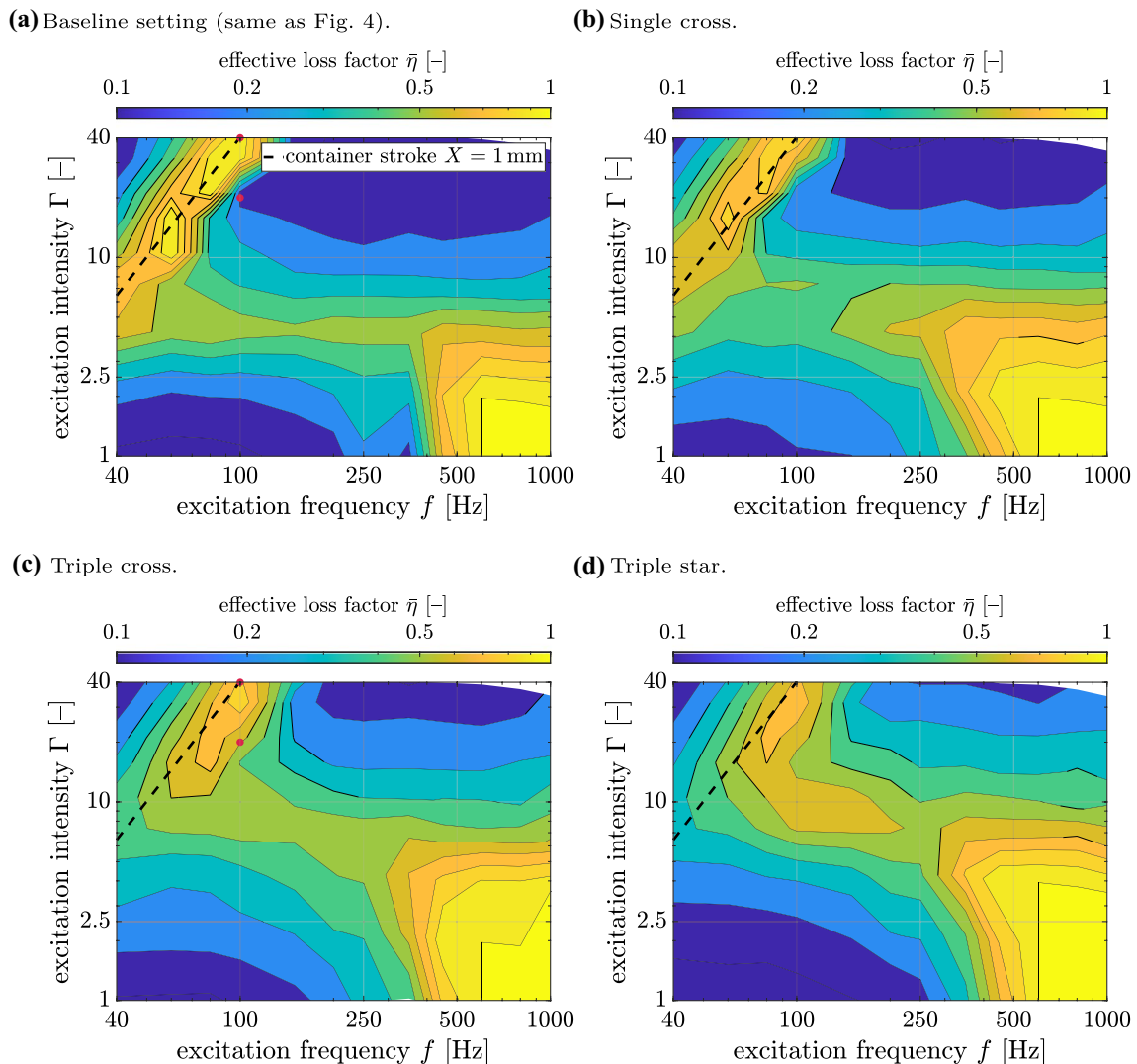


**Fig. 7** Effective loss factors of particle dampers with inner structures filled with steel particles of 1.25 mm radius and clearance  $h = \pi$  mm



the triple star setting. On the other hand, the gradient of the effective loss factor towards lower container strokes as the optimal stroke, i.e.  $X < X_{\text{opt}}$  (below the dashed line) strongly decreases with more inner structures being used. Thus, the particle damper becomes more robust in this excitation area. Note, this is only true for excitation intensities  $\Gamma > 7$ . Similarly, the effective loss factor increases faster at high excitation frequencies  $f > 500$  Hz the more inner structures are used. Especially at low excitation intensities  $\Gamma < 4$ , high effective loss factor values up to  $\bar{\eta} = 2.0$  are achieved for the triple star structure.

In contrast to the baseline setting, a smaller particle radius now has a big effect on the effective loss factor. In Fig. 8 the experimentally obtained effective loss factor is compared for a particle radius of 0.3 mm with and without the triple star inner structure but same clearance  $h = \pi$  mm.

It is seen that a smaller particle radius increases the effect of the inner structure, compare to Fig. 7d. While in the bouncing collect-and-collide motion mode the maximum effective loss factor further decreases to  $\bar{\eta} = 0.6$ , at high excitation frequencies a very large efficient area is seen. It ranges from excitation frequencies  $f > 400$  Hz and excitation intensities  $\Gamma \leq 10$ .

The aforementioned observations can be summarized with three simple rules of thumb:

- Inner structures lead to lower effective loss factors within the bouncing collect-and-collide motion mode, but to a more robust (less sensitive) behavior in this excitation area.
- Inner structures lead to higher effective loss factors at high frequencies.

- The more inner structures are used and the smaller the particle radius, the stronger the effect on the effective loss factor.

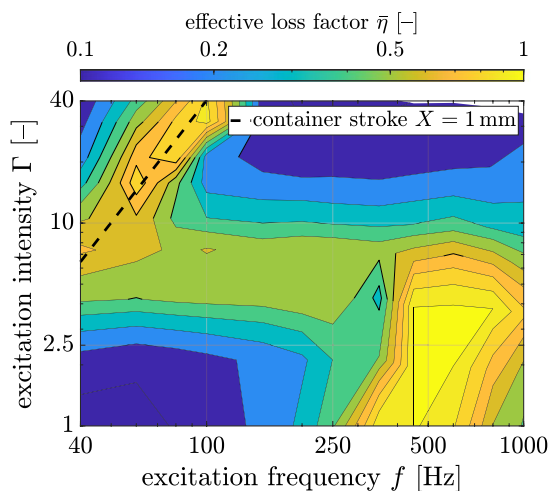
#### 4.2.2 Numerical insights

To obtain insights into the effect of the inner structures, these are also analyzed numerically for the triple cross setting. At first, the effect on the bouncing collect-and-collide motion mode is discussed. In Fig. 9 the velocity fields are shown for the baseline setting and the triple cross setting for a particle radius of 1.25 mm, an excitation frequency of  $f = 100$  Hz and an excitation intensity of both  $\Gamma = 20$  and  $\Gamma = 40$ . This marks the transition from low to high effective loss factor values, see also red marks in Fig. 7. The corresponding experimental and numerical effective loss factor values are summarized in Table 2. The velocity fields show the in-plane particle velocity in the direction of excitation and gravity, i. e. the  $x - y$  plane, see Fig. 2. An offset in  $z$ -direction of 3 mm is used to reduce the visibility of the inner

**Table 2** Effective loss factor values of baseline setting and triple cross setting at an excitation frequency of  $f = 100$  Hz and an excitation intensity of both  $\Gamma = 20$  and  $\Gamma = 40$  and clearance  $h = \pi$  mm

	Effective Loss Factor $\bar{\eta}$ [–]			
	Base Line		Triple cross	
	$\Gamma = 20$	$\Gamma = 40$	$\Gamma = 20$	$\Gamma = 40$
Experiment	0.17	1.0	0.64	0.81
Simulation	0.13	0.98	0.43	0.74

**(a)** Without inner structure.



**(b)** Triple star inner structure.

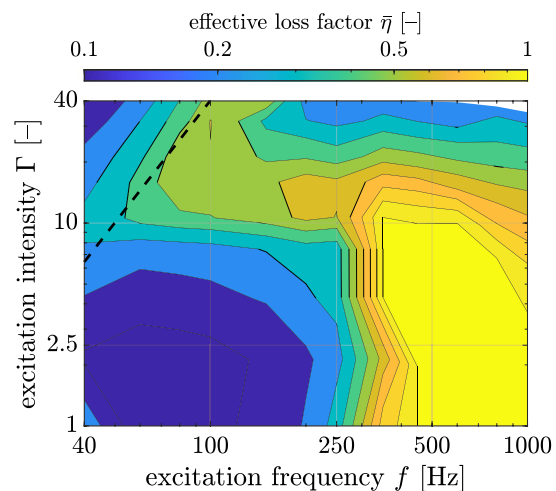
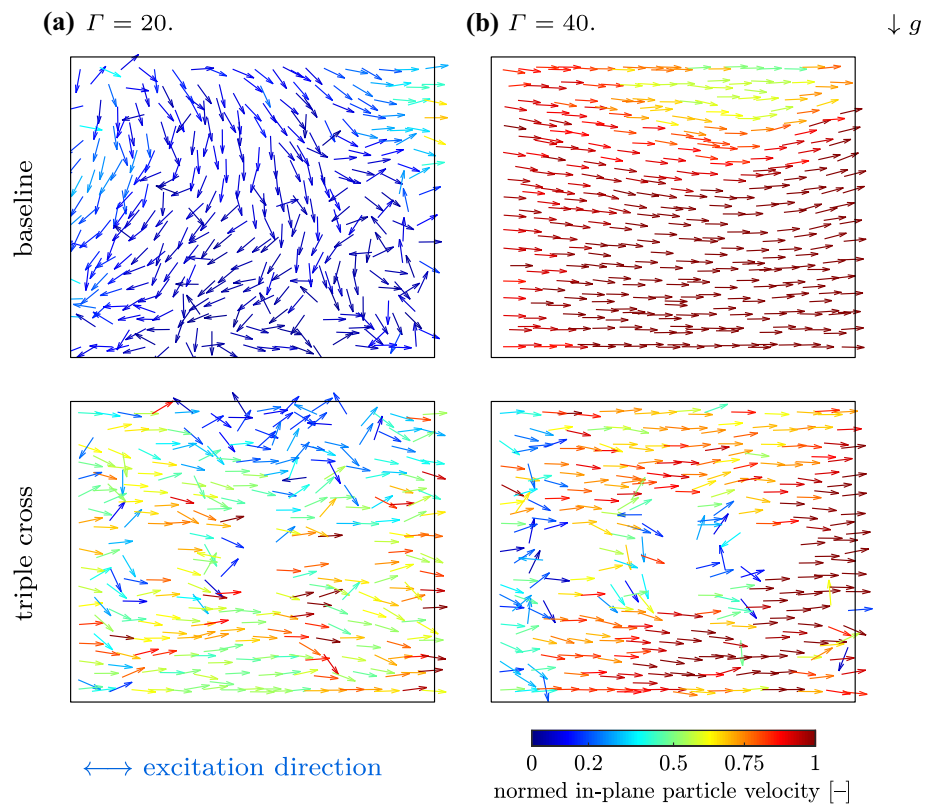


**Fig. 8** Comparison of effective loss factor for a steel particle radius of 0.3 mm for system with and without triple star inner structures and clearance  $h = \pi$  mm

**Fig. 9** Velocity fields of absolute particle velocity of red dots shown in Fig. 7 at a container position of  $x_c = X$ . The colors show the magnitude of the in-plane particle velocity normed by the container velocity amplitude  $V$  from low (blue) to high (red)



structure, which can be seen as white areas in the velocity fields.

The effective loss factor values of experiment and simulation fit well for the considered excitation conditions. Only for the triple cross and  $\Gamma = 20$  a significant difference can be observed. It is nevertheless assumed that the numerical model captures the qualitative dynamical behavior of the particles for all settings. Comparing the velocity field of the baseline setting with the triple cross setting at  $\Gamma = 40$ , see Fig. 9b, only small differences are seen. In the baseline setting the particles are unobstructed in their movement, resulting in a high particle velocity. Whereas for the triple cross setting, the mean particle velocity decreases slightly. Additionally, around the inner structure and on the left side of the particle block much lower velocities are achieved. This lowers the effective loss factor from  $\bar{\eta} = 1.0$  to  $\bar{\eta} = 0.81$ . In contrast to that, at  $\Gamma = 20$  the baseline setting shows only very little particle movement resulting in a low effective loss factor  $\bar{\eta} = 0.17$ , see Fig. 9b. This happens because the clearance  $h$  is too big and therefore no synchronized movement between particle bed and container is achieved, see the work of Sack et al. [28] for further discussion of this topic. By using an inner structure, the classical definition of the clearance during testing vanishes, as some particles get hindered by the structure. This leads to the effect that the bouncing collect-and-collide motion mode stays active even for container strokes of  $X < X_{\text{opt}}$ . However, the particle

velocity is reduced compared to the optimal stroke, which results in a decrease of the effective loss factor from  $\bar{\eta} = 0.81$  to  $\bar{\eta} = 0.64$ . However, this value is still much bigger than the baseline setting with  $\bar{\eta} = 0.17$ .

An accurate numerical analysis at high excitation frequencies  $f > 500$  Hz is not possible as the utilized numerical model is rather inaccurate in that area [21]. As the kinetic energy of the particle bed is very low in that area, resulting in only very little relative motion between the particles, this gives cause to conclude that the inner structures might lead to a higher energy transition onto the particles, which can then dissipate. Thus, more inner structures yield in higher energy dissipation. However, this assumption needs further investigations.

### 4.3 Coated container walls

Using inner structures, it is possible to tune the effective loss factor in a targeted manner. However, at low to medium excitation frequencies  $f < 250$  Hz and low to medium excitation intensities  $\Gamma < 5$  low effective loss factor values are still obtained, see e. g. Fig. 7. As seen in Fig. 4, for these settings the particle bed is in the local-fluidization or global-fluidization mode. Therefore, especially the lower particles show only little relative motion which can be seen in Fig. 1. As demonstrated in the last section, even inner structures are not able to increase the relative motion in this excitation

area. Hence, a different approach is necessary to increase the efficiency here.

The idea is to equip the container walls in longitudinal direction, i.e. in direction of excitation, with a *coating material*, to achieve a similar motion as in the bouncing collect-and-collide state. Within the bouncing collect-and-collide state, the particle bed takes-off the container base and moves through the container as one particle block. Now, the particle bed stays on the container's base and penetrates the coated wall as one block, see Fig. 10.

When this material is completely compressed, an inelastic collision with the wall occurs and the relative velocity between particle block and wall vanishes. This produces a new particle motion, henceforth referred to as *compression collect-and-collide*.

Various measurements have shown that a high effective loss factor is achieved at low excitation intensities for wall thicknesses of 3 mm. This is shown by example in Fig. 11 for a particle radius of 1.25 mm, coating wall Young's moduli of both 1.4 MPa and 55 MPa, and a clearance of  $h = \pi$  mm.

**Fig. 10** Particle movement for the compression collect-and-collide motion mode at high effective loss factor values, one particle chain

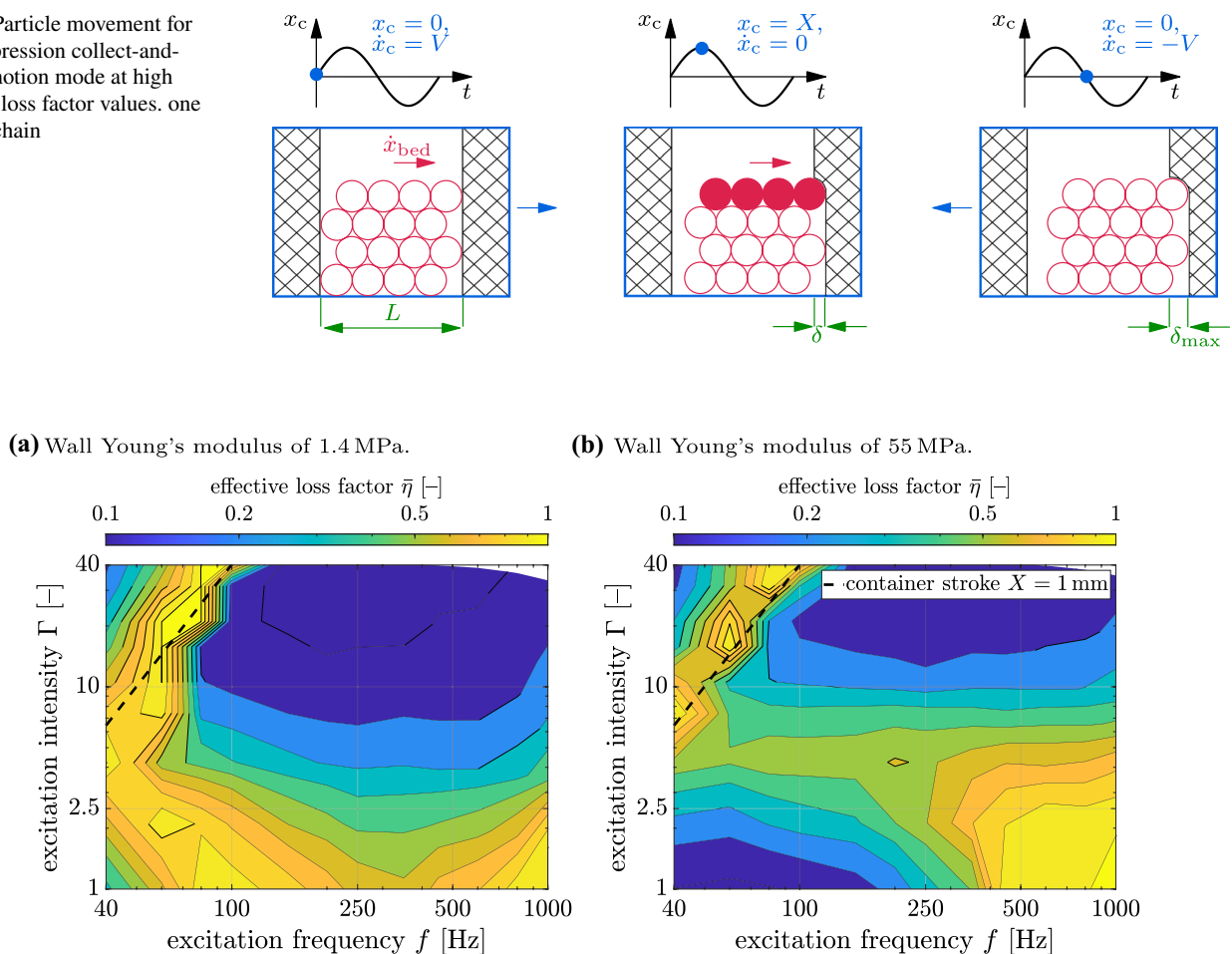


**Fig. 11** Experimental effective loss factors for coated wall system with different wall Young's moduli, a particle radius of 1.25 mm and a clearance of  $h = \pi$  mm

Compare the results also to the baseline setting in Fig. 4. For the weaker wall Young's modulus of 1.4 MPa, additional high effective loss factor values are obtained around an excitation frequency of  $f = 100$  Hz and  $\Gamma \leq 2.5$  with a decrease in excitation frequency towards higher excitation intensities. For the stronger wall Young's modulus of 55 MPa, additional high effective loss factor values around an excitation frequency of  $f = 500$  Hz and  $\Gamma \leq 2.5$  are seen. Hence, the frequency at high effective loss factors and low excitation intensities  $\Gamma \leq 2.5$  is strongly dependent on the coating wall material.

The following objective is to find a systematic formula to efficiently design the coating wall material. The focus lies on the excitation region which showed the most effects in the experiments when coating the walls, i.e. at low excitation intensities. It is found that the compression collect-and-collide state mainly depends on the compression depth of the coated material. Hence, an empirical formula based on the Hertz impact theory [9] shall be derived to design the coating wall material. Hertz theory assumes that both contact

partners are touching at a single point and all elastic deformation is limited to the contact point. From Hertz's theory the maximum penetration depth  $\delta_{\max}$  follows by Barber [3] to

$$\delta_{\max} = \left( \frac{5 \bar{M} V_0^2}{4 k_n} \right)^{2/5}, \quad (12)$$

with  $V_0$  being the initial collision velocity. For reasons of simplification it is assumed here that  $V_0 = V$ , i. e. the relative velocity at impact point corresponds to the maximum container velocity. The contact stiffness  $k_n$  can be expressed as

$$k_n = \frac{4}{3} \bar{E} \sqrt{\bar{R}}. \quad (13)$$

The effective Young's modulus  $\bar{E}$  is given by

$$\frac{1}{\bar{E}} = \frac{1 - \nu_p^2}{E_p} + \frac{1 - \nu_w^2}{E_w}, \quad (14)$$

with Young's modulus  $E_{p/w}$  and Poisson's ratio  $\nu_{p/w}$  of particle and wall respectively. The effective radius  $\bar{R}$  can be obtained by

$$\frac{1}{\bar{R}} = \frac{1}{r_p} + \frac{1}{r_w}, \quad (15)$$

with radius  $r_{p/w}$  of particle and wall. As the wall radius is infinite it follows  $\bar{R} = r_p$ . The effective mass  $\bar{M}$  is given by

$$\frac{1}{\bar{M}} = \frac{1}{m_p} + \frac{1}{m_w}, \quad (16)$$

with mass  $m_{p/w}$  of particle and wall respectively. As the container wall is driven by the shaker, its mass can be assumed to be infinitely large. Additionally, instead of a single particle a whole particle layer "impacts" the coated wall, see solid particle line in Fig. 10. Hence, the particle mass is adjusted by the number of particles in one line  $n_p^{\text{line}}$ . Thus,  $\bar{M} = n_p^{\text{line}} m_p$  is obtained.

Within the bouncing collect-and-collide state there exist a direct correlation between optimal container stroke  $X_{\text{opt}}$  and clearance  $h$ , i.e.  $X_{\text{opt}} = h/\pi$ , see Eq. (11). A similar correlation is found empirically for the compression collect-and-collide state. Indeed, here the clearance  $h$  is represented by the maximum compression of the coating wall material  $\delta_{\max}$ , see also Fig. 10. Empirically, the correlation

$$X = \delta_{\max}. \quad (17)$$

is found at the high effective loss factor values. This formula matches with the high effective loss factors in Fig. 11 for the compression collect-and-collide state. Hence, Eq. (17) can be solved conjointly with Eq. (12) in order to obtain the necessary effective Young's modulus of the coating material

$$\bar{E} = \frac{15 \bar{M} V^2}{16 \sqrt{\bar{R}} X^{5/2}}. \quad (18)$$

By inserting for the container amplitude  $X = A/\Omega^2$  and for the container velocity amplitude  $V = A/\Omega$ , the equation for the effective Young's modulus of the coating material follows to

$$\bar{E} = \frac{15 \bar{M} \Omega^3}{16 \sqrt{A \bar{R}}}. \quad (19)$$

Lastly, from the experiments presented in Fig. 11 a high efficiency of the compression collect-and-collide is observed at an excitation intensity  $\Gamma = 1$  which implies an acceleration amplitude of  $A = g$ . This finally results in

$$\bar{E} = \frac{15 n_p^{\text{line}} m_p \Omega_d^3}{16 \sqrt{g r_p}}, \quad (20)$$

with  $\Omega_d = 2\pi f_d$  being the wanted excitation frequency of high effective loss factor values at  $\Gamma = 1$ . From the effective Young's modulus by Eq. (20), the coating wall Young's modulus by Eq. (14) can be solved for. In the later experiments, it turned out that Young's moduli values in the range of polymers are obtained. Hence, the Poisson's ratio is assumed to be  $\nu_w = 0.5$ . For such low Young's moduli values the impact theory of Hertz is losing accuracy, as large deformations in the contact zone occur and thus the assumption of contact at a single point is not fulfilled anymore. Additionally, polymers generally behave in a visco-elastic manner instead of purely elastic. Therefore, Eq. (20) can only be seen as a rough estimation for the necessary Young's modulus of the coating wall material. This is likewise true as Eq. (20) is based on Eq. (17), which is based on empirical experimental observations.

Even though, the necessary Young's modulus of the coating wall can be obtained now, the particle damper can not be considered as robust, see Fig. 11. This is because the high effective loss factor values of the compression collect-and-collide and bouncing collect-and-collide states do not occur at the same vibration frequency. The goal is to adjust the effective loss factor of the bouncing collect-and-collide motion mode in such a manner that it fits the desired excitation frequency of the compression collect-and-collide motion mode. Measurements have shown that a good match is achieved if the clearance for the bouncing collect-and-collide state is adjusted to match an excitation intensity at  $\Gamma = 15$  at the desired excitation frequency  $\Omega_d$ . Hence, the clearance follows from Eq. (11) to

$$h = \pi X_{\text{opt}} = \pi \frac{A_{\text{opt}}}{\Omega_d^2} = \pi \frac{15 g}{\Omega_d^2}. \quad (21)$$

### 4.3.1 Validation

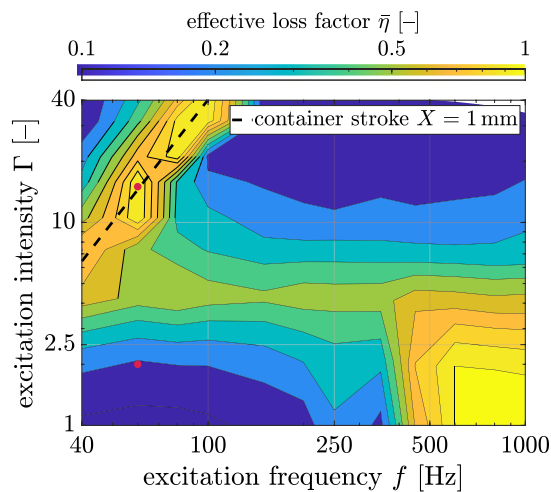
To validate the presented design approach, it is applied to design a particle damper for excitation frequencies of  $f = 50$  Hz, 60 Hz and 80 Hz, respectively. The calculated and used parameters for these tests are summarized in Table 3 and the results are shown in Fig. 12.

**Table 3** Settings of coated wall experiments

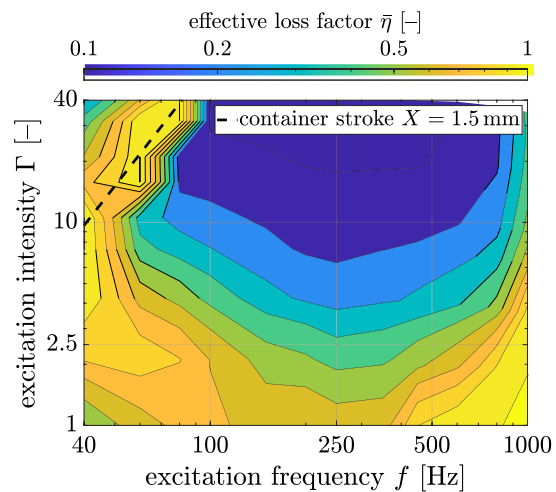
Frequency $f$ [Hz]	50	60	80
Clearance $h$ [mm]	4.8	3.3	1.9
Optimal Stroke $X_{\text{opt}}$ [mm]	1.5	1.1	0.6
$E_w$ [MPa] (by Eq. (20))	0.25	0.44	1.0
$E_w$ [MPa] (used)	0.27	0.72	1.4

For each configuration, a very robust behavior of the effective loss factor concerning the excitation intensity at the desired excitation frequency is achieved. This range of excitation intensities almost extends over the whole measurement range of  $\Gamma = 1 - 40$ . For excitation frequencies below and above the desired one, a medium reduction in the effective loss factor is seen. However, at medium to high excitation frequencies  $f > 200$  Hz, no improvement in comparison to the baseline setting is achieved. First measurements at even higher excitation frequencies  $f > 1000$  Hz indicate a very high effective loss factor. This tendency can already be seen in Fig. 12 but needs further investigations.

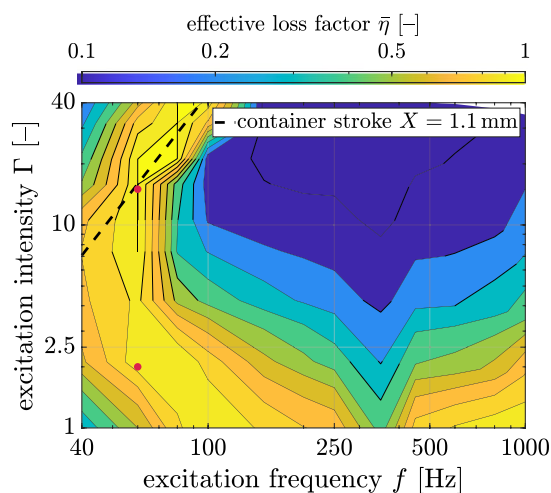
**(a)** Baseline setting (same as Fig. 4).



**(b)** Designed for  $f = 50$  Hz.



**(c)** Designed for  $f = 60$  Hz.



**(d)** Designed for  $f = 80$  Hz.

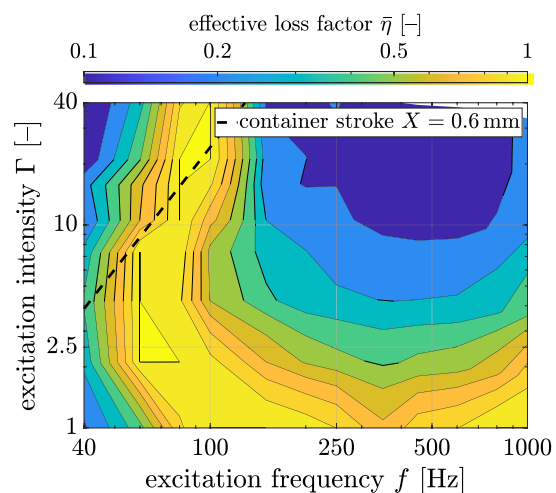


**Fig. 12** Effective loss factors for particle dampers with coated walls designed for different excitation frequencies. The design parameters are summarized in Table 3



### 4.3.2 Numerical insights

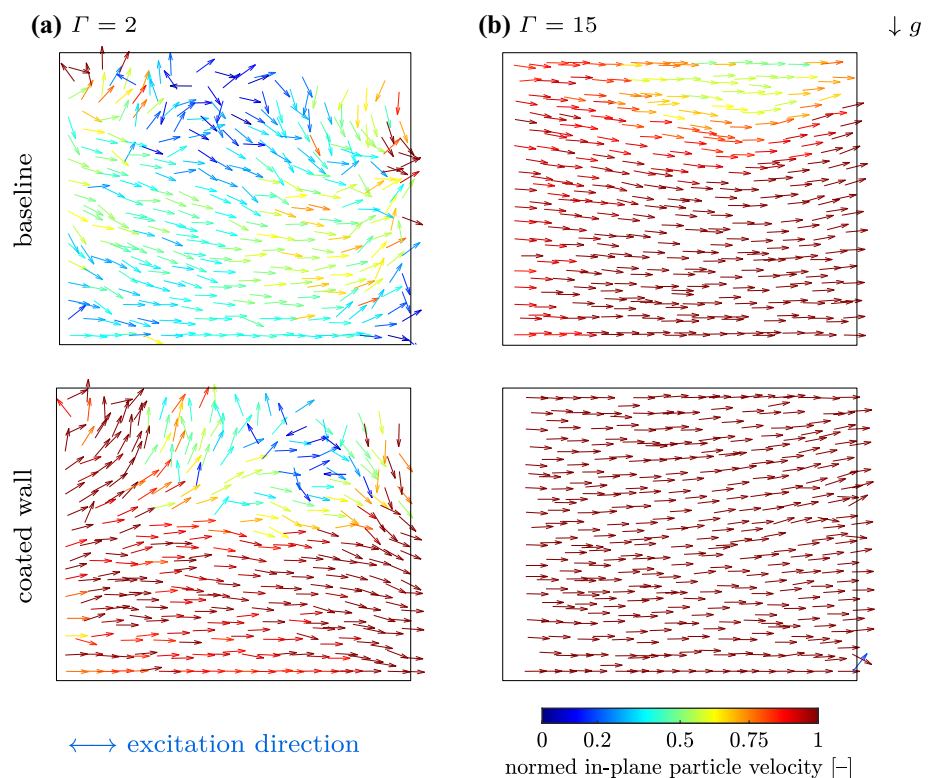
To obtain deeper insights into the particle motion using coated walls, numerical studies using DEM are performed for a particle radius of  $r = 1.25$  mm. In the following, the bouncing collect-and-collide and compression collect-and-collide motion mode for an excitation frequency of  $f = 60$  Hz and excitation intensities of  $\Gamma = 2$  and  $\Gamma = 15$  are studied for a wall Young's modulus of  $E_w = 0.72$  MPa, see also red marks in Fig. 12. The effective loss factors obtained from simulations and experiments are summarized in Table 4. Experimental and numerical values are in the same range, showing the qualitative agreement. However, quantitatively there is some mismatch for the low excitation intensities. Despite this, it can be assumed that the overall dynamical behavior of the particles is reproduced by simulation. The corresponding velocity fields extracted from simulations are displayed in Fig. 13.

**Table 4** Effective loss factor values of red dots shown in Fig. 12

	Base Line		Coated Wall	
	$\Gamma = 2$	$\Gamma = 15$	$\Gamma = 2$	$\Gamma = 15$
Experiment	0.20	1.0	0.97	1.4
Simulation	0.41	0.96	0.64	1.1

The baseline setting is in the local-fluidization mode for  $\Gamma = 2$ . While the upper particles move at a high velocity, particles in the middle and at the bottom are comparably slow, i. e. the whole particle block does not take-off the container's base. This results in a low effective loss factor of  $\bar{\eta} = 0.2$ . In the coated wall system, the upper particles also show high velocities. The middle and bottom particles, however, are moving as one particle block with an even higher velocity. This particle system does not take off the container's base either. Though, as the container's wall gets compressed, a relative motion between container and particle block is possible. Hence, a high effective loss factor of  $\bar{\eta} = 0.97$  is achieved in the experiments. At  $\Gamma = 15$  the bouncing collect-and-collide motion mode is observed for both settings, i. e. baseline setting and coated wall setting. Here, the particle bed takes-off the container base and moves with a high velocity as one particle block. In both cases, this results in a high effective loss factors. Interestingly, the coated wall system reaches even higher particle velocities than the baseline setting. Consequently, its effective loss factor value is higher, i. e.  $\bar{\eta} = 1.4$  to  $\bar{\eta} = 1.0$  for  $\Gamma = 15$ . This means that the bouncing collect-and-collide motion mode is more efficient for the coated wall setting than for the base line setting.

**Fig. 13** Velocity fields of absolute particle velocity of baseline setting and coated wall setting at  $x_c = X$  of red dots in Fig. 12. The colors show the magnitude of the in-plane particle velocity normed by the container velocity amplitude  $V$  from low (blue) to high (red)



## 5 Conclusion

The efficiency of classical particle dampers is sensitive to the excitation frequency and excitation amplitude. Thus, during the design process of these dampers, the excitation conditions have to be known quite accurately, which is rarely feasible for real industrial applications. Hence, to obtain a robust particle damper, two different design approaches are discussed in this paper. While experimental measurements are carried out for analysis, numerical studies using the discrete element method are used to obtain deeper insights into the dynamical effects of the new damper designs.

The first design approach uses inner structures inside the particle container. The inner structures are manufactured using a SLA 3D printer and consist of different numbers of beams placed perpendicularly to the container motion. These inner structures yield lower effective loss factors of the bouncing collect-and-collide motion mode, but also to a more robust behavior. At high excitation frequencies, higher effective loss factors are achieved. These effects can even be increased by using more inner structures or a smaller particle radius. It is concluded that inner structures are especially suitable when damping on a large excitation range or at high frequencies is necessary.

The second design approach uses coated container walls to increase the damping performance. A new motion mode, called compression collect-and-collide, is observed within this setting. In traditional particle dampers at low excitation frequencies and low excitation intensities, only little relative motion between particle bed and container is seen. In the coated container instead, the wall gets compressed, resulting in a high relative motion between particles and container and thus a reasonable energy dissipation is achieved. An analytical formula based on Hertz's impact theory is derived to design the coating wall material. The formulas accuracy is proven experimentally. By adjusting the bouncing collect-and-collide motion mode to fit the compression collect-and-collide motion mode, a very robust damper at low excitation frequencies is achieved. Additionally, the efficiency of the bouncing collect-and-collide motion mode is increased. However, the damper's efficiency at medium and high excitation frequencies is not affected.

**Acknowledgements** The authors would like to thank the German Research Foundation (DFG) for the financial support of the project 424825162. The authors would also like to thank Dr.-Ing. Marc-André Pick, Dipl.-Ing. Riza Demir, Dipl.-Ing. Norbert Borngreber-Sander and Wolfgang Brennecke for helping to design and realize the experimental rig.

**Funding** Open Access funding enabled and organized by Projekt DEAL.

## Declarations

**Conflicts of interest** On behalf of all authors, the corresponding author states that there is no conflict of interest.

**Open Access** This article is licensed under a Creative Commons Attribution 4.0 International License, which permits use, sharing, adaptation, distribution and reproduction in any medium or format, as long as you give appropriate credit to the original author(s) and the source, provide a link to the Creative Commons licence, and indicate if changes were made. The images or other third party material in this article are included in the article's Creative Commons licence, unless indicated otherwise in a credit line to the material. If material is not included in the article's Creative Commons licence and your intended use is not permitted by statutory regulation or exceeds the permitted use, you will need to obtain permission directly from the copyright holder. To view a copy of this licence, visit <http://creativecommons.org/licenses/by/4.0/>.

## References

- Andersson, S., Söderberg, A., Björklund, S.: Friction models for sliding dry, boundary and mixed lubricated contacts. *Tribol. Int.* **40**(4), 580–587 (2007). <https://doi.org/10.1016/j.triboint.2005.11.014>
- Bannerman, M.N., Kollmer, J.E., Sack, A., Heckel, M., Mueller, P., Pöschel, T.: Movers and shakers: granular damping in microgravity. *Phys. Rev. E* (2011). <https://doi.org/10.1103/PhysRevE.84.011301>
- Barber, J.R.: *Contact Mechanics. Solid Mechanics and Its Applications*. Springer, Cham (2018). <https://doi.org/10.1007/978-3-319-70939-0>
- Cundall, P.A., Strack, O.D.L.: A discrete numerical model for granular assemblies. *Int. J. Rock Mech. Min. Sci. Geomech.* **16**(4), 47–65 (1979). <https://doi.org/10.1680/geot.1979.29.1.47>
- Gear, C.W.: The numerical integration of ordinary differential equations of various orders. *Math. Comput.* **21**(98), 146 (1967). <https://doi.org/10.2307/2004155>
- Gnanasambandham, C., Fleissner, F., Eberhard, P.: Enhancing the dissipative properties of particle dampers using rigid obstacle-grids. *J. Sound Vib.* **484**, 115522 (2020). <https://doi.org/10.1016/j.jsv.2020.115522>
- Gnanasambandham, C., Stender, M., Hoffmann, N., Eberhard, P.: Multi-scale dynamics of particle dampers using wavelets: extracting particle activity metrics from ring down experiments. *J. Sound Vib.* **454**, 1–13 (2019). <https://doi.org/10.1016/j.jsv.2019.04.009>
- Gonthier, Y., McPhee, J., Lange, C., Piedbœuf, J.C.: A regularized contact model with asymmetric damping and dwell-time dependent friction. *Multibody Syst. Dyn.* **11**(3), 209–233 (2004). <https://doi.org/10.1023/B:MUBO.0000029392.21648.bc>
- Hertz, H.: *The principles of Mechanics: Presented in a New Form, Unabridged and Unaltered Republication of the 1 edn*. Dover Books. Dover Publications, New York (1956)
- Hollkamp, J.J., Gordon, R.W.: Experiments with particle damping. In: *Proceedings Volume 3327, Smart Structures and Materials 1998: Passive Damping and Isolation* (1998). <https://doi.org/10.1117/12.310675>
- Johnson, C.D.: Design of passive damping systems. *J. Mech. Design* **117**, 171–176 (1995). <https://doi.org/10.1115/1.2838659>
- Li, K., Darby, A.P.: A buffered impact damper for multi-degree-of-freedom structural control. *Earthq. Eng. Struct. Dyn.* **37**(13), 1491–1510 (2008). <https://doi.org/10.1002/eqe.823>
- Lu, G., Third, J.R., Müller, C.R.: Discrete element models for non-spherical particle systems: from theoretical developments to

- applications. *Chem. Eng. Sci.* **127**, 425–465 (2015). <https://doi.org/10.1016/j.ces.2014.11.050>
14. Lu, Z., Lu, X., Lu, W., Masri, S.: Experimental studies of the effects of buffered particle dampers attached to a multi-degree-of-freedom system under dynamic loads. *J. Sound Vib.* **331**, 2007–2022 (2012). <https://doi.org/10.1016/J.JSV.2011.12.022>
  15. Masmoudi, M., Job, S., Abbes, M.S., Tawfiq, I., Haddar, M.: Experimental and numerical investigations of dissipation mechanisms in particle dampers. *Granul Matter* **18**(3), 71 (2016). <https://doi.org/10.1007/s10035-016-0667-4>
  16. Matuttis, H.G.: *Understanding the Discrete Element Method: Simulation of Non-Spherical Particles for Granular and Multi-Body Systems*. Wiley, Singapore (2014). <https://doi.org/10.1002/9781118567210>
  17. Meyer, N., Schwartz, C., Morlock, M., Seifried, R.: Systematic design of particle dampers for horizontal vibrations with application to a lightweight manipulator. *J. Sound Vib.* **510**, 116319 (2021). <https://doi.org/10.1016/j.jsv.2021.116319>
  18. Meyer, N., Seifried, R.: Experimental and numerical investigations on parameters influencing energy dissipation in particle dampers. In: VI International Conference on Particle-based Methods—Fundamentals and Applications pp. 260–271 (2019)
  19. Meyer, N., Seifried, R.: An experimental model for the analysis of energy dissipation in particle dampers. *Proc. Appl. Math. Mech. (PAMM)* (2019). <https://doi.org/10.1002/pamm.201900171>
  20. Meyer, N., Seifried, R.: Numerical and experimental investigations in the damping behavior of particle dampers attached to a vibrating structure. *Comput. Struct.* **238**, 106281 (2020). <https://doi.org/10.1016/j.compstruc.2020.106281>
  21. Meyer, N., Seifried, R.: Toward a design methodology for particle dampers by analyzing their energy dissipation. *Comput. Particle Mech.* **8**(4), 681–699 (2021). <https://doi.org/10.1007/s40571-020-00363-0>
  22. Meyer, N., Seifried, R.: Energy dissipation in horizontally driven particle dampers of low acceleration intensities. *Nonlinear Dyn.* **108**, 3009–3024 (2022). <https://doi.org/10.1007/s11071-022-07348-z>
  23. Meyer, N., Wagemann, E.L., Jackstadt, A., Seifried, R.: Material and particle size sensitivity analysis on coefficient of restitution in low-velocity normal impacts. *Comput. Particle Mech.* (2022). <https://doi.org/10.1007/s40571-022-00471-z>
  24. Paget, A.L.: Vibration in steam turbine buckets and damping by impacts. *Engineering* **143**, 305–307 (1937)
  25. Panossian, H.: Non-obstructive particle damping experience and capabilities. In: *Proceedings of SPIE—The International Society for Optical Engineering*, vol. 4753. pp. 936–941 (2002). <https://doi.org/10.2514/6.2008-2102>
  26. Pöschel, T.: *Computational Granular Dynamics: Models and Algorithms*. Springer, Berlin (2005). <https://doi.org/10.1007/3-540-27720-X>
  27. Pourtavakoli, H., Parteli, E.J.R., Pöschel, T.: Granular dampers: Does particle shape matter? *New J. Phys.* **18**(7), 073049 (2016). <https://doi.org/10.1088/1367-2630/18/7/073049>
  28. Sack, A., Heckel, M., Kollmer, J., Zimmer, F., Pöschel, T.: Energy dissipation in driven granular matter in the absence of gravity. *Phys. Rev. Lett.* (2013). <https://doi.org/10.1103/PhysRevLett.111.018001>
  29. Saluena, C., Esipov, S.E., Poeschel, T., Simonian, S.S.: Dissipative properties of granular ensembles. *Proceedings of SPIE Volume 3327, Smart Structures and Materials 1998: Passive Damping and Isolation* pp. 23–29 (1998). <https://doi.org/10.1117/12.310696>
  30. Sanchez, M., Rosenthal, G., Pugnali, L.: Universal response of optimal granular damping devices. *J. Sound Vib.* **331**(20), 4389–4394 (2012). <https://doi.org/10.1016/j.jsv.2012.05.001>
  31. Schönle, A., Gnanasambandham, C., Eberhard, P.: Broad-band damping properties of particle dampers mounted to dynamic structures. *Exp. Mech.* (2022). <https://doi.org/10.1007/s11340-022-00882-2>
  32. Simonian, S.S.: Particle beam damper. *Proceedings of SPIE Volume 2445, Smart Structures and Materials 1995: Passive Damping*, pp. 149–160 (1995). <https://doi.org/10.1117/12.208884>
  33. Wong, C., Spencer, A., Rongong, J.: Effects of enclosure geometry on particle damping performance. In: *Proceedings of the 50th AIAA/ASME/ASCE/AHS/ASC Structures, Structural Dynamics, and Materials Conference* (2009). <https://doi.org/10.2514/6.2009-2689>
  34. Yang, M.Y., Lesieutre, G.A., Hambric, S., Koopmann, G.: Development of a design curve for particle impact dampers. *Noise Control Eng. J.* **53**, 5–13 (2005). <https://doi.org/10.1117/12.540019>
  35. Yao, B., Chen, B.: Investigation on zero-gravity behavior of particle dampers. *J. Vib. Control* **21**(1), 124–133 (2015). <https://doi.org/10.1177/1077546313488157>
  36. Yin, Z., Su, F., Zhang, H.: Investigation of the energy dissipation of different rheology behaviors in a non-obstructive particle damper. *Powder Technol.* (2017). <https://doi.org/10.1016/j.powtec.2017.07.090>
  37. Zhang, K., Chen, T., He, L.: Damping behaviors of granular particles in a vertically vibrated closed container. *Powder Technol.* **321**, 173–179 (2017). <https://doi.org/10.1016/j.powtec.2017.08.020>

**Publisher's Note** Springer Nature remains neutral with regard to jurisdictional claims in published maps and institutional affiliations.